

## Optimization of the thermoelectric properties in self-substituted Fe<sub>2</sub>VAl

E. Alleno<sup>1,\*</sup>, A. Diack-Rasselio<sup>1</sup>, M. S. Talla Noutack<sup>2</sup>, and P. Jund<sup>2</sup>

<sup>1</sup>Univ. Paris Est Creteil, CNRS, ICMPE, UMR 7182, 2-8, rue H. Dunant, F-94320 THIAIS, France

<sup>2</sup>ICGM, Université Montpellier, CNRS, ENSCM, Montpellier, France



(Received 10 January 2023; revised 9 June 2023; accepted 26 June 2023; published 21 July 2023)

Thermoelectric properties were determined in self-substituted Fe<sub>2</sub>VAl Heusler alloys (Fe<sub>2</sub>V<sub>1+x</sub>Al<sub>1-x</sub>,  $-0.1 < x < 0.1$ ), pursuing the goal of their optimization. A parabolic band model fitted to experimental plots of Seebeck coefficient versus charge carrier concentration at 220 K yielded values of the density of states (DOS) effective mass,  $m_v^* = 3.2m_e$  and  $m_c^* = 13.7m_e$  for the holes and electrons, respectively ( $m_e$  is the bare electron mass). The measured Sommerfeld coefficient of the electronic specific heat is consistently smaller in *p*-type Fe<sub>2</sub>V<sub>0.92</sub>Al<sub>1.08</sub> ( $\gamma_p = 7.8 \text{ mJ mol}^{-1} \text{ K}^{-2}$ ) than in *n*-type Fe<sub>2</sub>V<sub>1.07</sub>Al<sub>0.93</sub> ( $\gamma_n = 11.5 \text{ mJ mol}^{-1} \text{ K}^{-2}$ ). First-principles calculations of the DOS lead to the theoretical values  $m_v^* = 2.4m_e$ ,  $m_c^* = 13.0m_e$ , and  $\frac{\gamma_n}{\gamma_p} = 1.9$ , in good agreement with the experimental values. These direct comparisons of calculations with experiments unambiguously show that the heavy electrons arise from flat Fe  $e_g$  conduction bands. Calculations of the optimum thermoelectric power factor (*PF*) show that it is nearly reached experimentally in *n*-type Fe<sub>2</sub>V<sub>1.03</sub>Al<sub>0.97</sub> ( $PF = 6.6 \text{ mW m}^{-1} \text{ K}^{-2}$  for  $n = 1.4 \times 10^{21} \text{ cm}^{-3}$ ) whereas *p*-type Fe<sub>2</sub>V<sub>0.985</sub>Al<sub>1.015</sub> ( $PF = 2.7 \text{ mW m}^{-1} \text{ K}^{-2}$  at  $p = 6.7 \times 10^{20} \text{ cm}^{-3}$ ) is not yet optimum. The easier optimization of the thermoelectric properties in *n*-type self-substituted Fe<sub>2</sub>VAl can be traced back to the larger effective DOS mass of its electrons.

DOI: [10.1103/PhysRevMaterials.7.075403](https://doi.org/10.1103/PhysRevMaterials.7.075403)

### I. INTRODUCTION

Thermoelectric devices can convert heat into electricity (Seebeck effect) or transfer heat under the influence of an electrical current (Peltier effect). These devices currently display a fairly small conversion efficiency (<10%), which is compensated by their very high reliability (no moving parts) and compactness. They are commercialized as refrigerators or envisaged as localized electric generators to power wireless sensors or to recycle the waste heat lost in industrial processes [1,2]. Their efficiency varies like the dimensionless figure of merit *ZT* of their constituting materials. *ZT* is defined by the expression  $ZT = \frac{\alpha^2 T}{\rho \lambda}$  with  $\alpha$  the Seebeck coefficient,  $\rho$  the electrical resistivity,  $\lambda$  the thermal conductivity, and  $T$  the absolute temperature. Bi<sub>2</sub>Te<sub>3</sub> is the material currently commercialized in thermoelectric refrigerators [3]. It displays a dimensionless figure of merit  $ZT \sim 1$  at 300 K, which is a landmark value rarely exceeded at this temperature [4,5]. Nevertheless, new thermoelectric materials should be developed because the scarcity and cost of tellurium prevent a mass-market development based on Bi<sub>2</sub>Te<sub>3</sub> in bulk form.

The Heusler alloy Fe<sub>2</sub>VAl could substitute Bi<sub>2</sub>Te<sub>3</sub> if its figure of merit was increased. It displays a power factor ( $PF = \frac{\alpha^2}{\rho}$ ) at least as large as in Bi<sub>2</sub>Te<sub>3</sub> ( $>5 \text{ mW m}^{-1} \text{ K}^{-2}$  at 300 K for *n*-type conduction), but its thermal conductivity is more than ten times larger in its pristine form ( $\lambda = 29 \text{ W m}^{-1} \text{ K}^{-1}$ ) [6]. Several research paths such as alloying and nanostructuring [7] have been undertaken to decrease

the lattice thermal conductivity and to increase the figure of merit. A maximum  $ZT = 0.2$  at 400 K has been obtained in micrograined Fe<sub>2</sub>VAl<sub>0.95</sub>Ta<sub>0.05</sub> [8] and more recently,  $ZT = 0.3$  was reached between 300 and 500 K in micrograined Fe<sub>2</sub>V<sub>0.95</sub>Ta<sub>0.05</sub>Al<sub>0.9</sub>Si<sub>0.1</sub> [9] and in nanograined Fe<sub>2</sub>VAl<sub>0.95</sub>Ta<sub>0.05</sub> [10]. These achievements are already significant, but further progress requires optimizing the power factor in Fe<sub>2</sub>VAl for both types of conduction.

Large values of maximum power factor (*PF*) are indeed already obtained in *n*-type Fe<sub>2</sub>VAl:  $PF_{\text{max}} = 6.8 \text{ mW m}^{-1} \text{ K}^{-2}$  at 300 K in both Fe<sub>1.98</sub>V<sub>1.02</sub>Al<sub>0.9</sub>Si<sub>0.1</sub> [11] and Fe<sub>2</sub>V<sub>0.95</sub>Ta<sub>0.05</sub>Al<sub>0.95</sub>V<sub>0.05</sub> [8], very recently  $PF_{\text{max}} = 7.5 \text{ mW m}^{-1} \text{ K}^{-2}$  in quenched Fe<sub>2</sub>VAl [12] or  $PF_{\text{max}} = 10.3 \text{ mW m}^{-1} \text{ K}^{-2}$  in Fe<sub>2</sub>V<sub>0.95</sub>Ta<sub>0.05</sub>Al<sub>0.9</sub>Si<sub>0.1</sub> [13]. But *p*-type Fe<sub>2</sub>VAl, for instance Fe<sub>2</sub>V<sub>0.985</sub>Al<sub>1.015</sub> [14] displays a smaller  $PF_{\text{max}} = 3.2 \text{ mW m}^{-1} \text{ K}^{-2}$  at 300 K. These values of power factors are not very well understood, and it is unknown yet if they are fully optimized. Recently, Anand *et al.* [15] reported in *n*- and *p*-type Fe<sub>2</sub>VAl large effective masses, favorable to high power factors. However, their determinations were not based on measured charge carrier concentrations. They rather assumed that the charge carrier concentrations can be derived from valence electron counts and that the transport parameters are independent of the nature of the dopant. Indeed, based on measured Seebeck coefficient and charge carrier concentration values, Garmroudi *et al.* very recently reported a large effective mass ( $m_c^* = 12.8m_e$ ) in *n*-type doped Fe<sub>2</sub>V<sub>1-x</sub>Ti<sub>x</sub>Al<sub>1-y</sub>Si<sub>y</sub> [16]. However, no hole effective mass, no optimization of the thermoelectric properties and more importantly, no direct comparison with first-principles calculations is reported in the previous study.

\*Corresponding author: eric.alleno@cnsr.fr

We hence focused our attention on the off-stoichiometric or “self-substituted”  $\text{Fe}_2\text{V}_{1+x}\text{Al}_{1-x}$  ( $-0.1 \leq x \leq 0.1$ ) series due to its chemical simplicity and because a large power factor  $PF_{\text{max}} = 6.8 \text{ mW m}^{-1} \text{ K}^{-2}$  at 300 K has been reported in  $n$ -type  $\text{Fe}_2\text{V}_{1+x}\text{Al}_{1-x}$  ( $0 \leq x \leq 0.1$ ) [14,17]. It is a better description of the actual crystal structure to write  $\text{Fe}_2\text{V}_{1+x}\text{Al}_{1-x}$  as  $\text{Fe}_2\text{V}(\text{Al}_{1-x}\text{V}_x)$  or  $\text{Fe}_2(\text{V}_{1-x}\text{Al}_x)\text{Al}$ , underlining the occurrence of  $\text{V}_{\text{Al}}$  or  $\text{Al}_{\text{V}}$  antisite defects. We recently extended this work by investigating the microstructural and thermoelectric properties of the  $\text{Fe}_{2+x}\text{VAl}_{1-x}$ , and  $\text{Fe}_{2-x}\text{V}_{1+x}\text{Al}$  ( $-0.1 \leq x \leq 0.1$ ) series [14], which also behave as solid solutions in this portion of the ternary phase diagram. However, the thermoelectric properties of the last two series were inferior to the former one. We thus hereby report a detailed investigation of the electronic transport properties of  $\text{Fe}_2\text{V}_{1+x}\text{Al}_{1-x}$  ( $-0.1 < x < 0.1$ ) by combining resistivity, Seebeck coefficient, and Hall effect measurements, firstly in a broad range of temperatures [100 – 600 K] and secondly focusing on the  $T = 220$  K temperature, as latter explained. This yields well-established values of Hall mobility and effective mass for both electrons and holes in  $\text{Fe}_2\text{VAl}$ . These effective masses are confirmed by specific heat measurements and directly compared to theoretical values obtained by first-principles calculations. The knowledge of these parameters allows a better understanding of the electronic transport in  $n$ - and  $p$ -type  $\text{Fe}_2\text{VAl}$ , of its relationships with the electronic structure, as well as determining newly and well-optimized values of charge carrier concentration and power factor for both types of conduction.

## II. EXPERIMENTAL AND THEORETICAL DETAILS

$\text{Fe}_2\text{V}_{1+x}\text{Al}_{1-x}$ , ( $x = -0.07, -0.05, -0.03, -0.015, 0.02, 0.03, 0.05, 0.08$ ),  $\text{Fe}_{2+x}\text{V}_{1-x}\text{Al}$  ( $x = 0.04, 0.08$ ) and  $\text{Fe}_{2+x}\text{VAl}_{1-x}$  ( $x = -0.08, 0.08$ ) samples were synthesized by melting the required amounts of iron (99.97%), vanadium (99.9%), and aluminum (99.98%) in an arc furnace under argon atmosphere. The resulting 2.5 g ingots were melted and flipped over at least four times to ensure homogeneity. Weight losses were less than 0.3%. This was followed by annealing in a quartz ampoule under vacuum at 900 °C for 72 h. Characterization by x-ray diffraction and electron probe microanalysis showed that these samples are fully single-phase and display an effective composition equal to the nominal one. More details on these characterizations of the microstructure can be found in Ref. [14]. Using a c-BN wheel saw,  $\sim 1$ -mm – thick disks were cut in the ingots (button-shaped) for resistivity measurements in the van der Pauw geometry. Constant thickness across the disk was reached by polishing. Bar-shaped samples were cut in the same disks for Seebeck coefficient and Hall effect measurements. Samples were systematically annealed again at 900 °C for 2 h to remove any cold-work effect arising from the cutting or polishing [18]. High and low-temperature resistivity and Seebeck coefficient measurements were carried out using two home-made setups [19,20]. Hall effect measurements were performed with a Physical Properties Measurement System (PPMS, Quantum Design) in AC mode by varying the magnetic field between -3 T and +3 T. The Hall electron or hole concentration and Hall electron mobility were defined by  $n$  or  $p = -\frac{1}{eR_H}$  and

$\mu_e = \frac{R_H}{\rho}$ , respectively, with  $R_H$  the Hall coefficient and  $e$  the elementary charge. Specific heat was measured also with a PPMS in the temperature range 2 – 25 K.

Calculations of the electronic structure were performed in the frame of the density functional theory (DFT) using the Vienna *ab initio* simulation package (VASP) [21,22] and the projector augmented waves (PAW) technique [23,24] within the generalized gradient approximation. The Perdew-Burke-Ernzerhof parameterization was applied [25,26] and standard versions of the PAW potentials for Fe ( $3p^6 3d^6 4s^2$ ), V ( $3s^2 3p^6 3d^3 4s^2$ ) and Al ( $3s^2 3p^1$ ) were used. The first Brillouin zone was sampled using a tight  $15 \times 15 \times 15$  Monkhorst-Pack  $k$ -point mesh [27] for the calculation of the density of states (DOS). The cutoff energy was set to 500 eV for the whole study. Both cell parameters and atomic positions were relaxed within an energy accuracy of 1  $\mu\text{eV}$  and  $10^{-5} \text{ eV/\text{Å}}$  for the forces before the calculation of the DOS. A  $3 \times 3 \times 3$  (108 atoms) supercell of the primitive unit cell of  $\text{Fe}_2\text{VAl}$  was used in this study. In this supercell, we considered either one or two antisites defects for each type ( $\text{V}_{\text{Al}}$  or  $\text{Al}_{\text{V}}$ ) leading to concentrations of 1.04 or 1.07 for the supernumerary element. Concerning the charge  $q$  of these defects, a systematic study of their formation energy for  $-6 \leq q \leq +6$ , similarly to what has been done in Ref. [28], showed not surprisingly that a  $\text{V}_{\text{Al}}$  antisite bears a charge  $q = +2$  whereas an  $\text{Al}_{\text{V}}$  antisite has a charge  $q = -2$ . A study of the most stable configuration of the supercells containing two antisites showed that a random distribution of the defects is favored (see Ref. [29] for more details on the methodology).

To determine the density of states effective mass  $m^*$  we have used the same procedure as the one described in detail in Ref. [30]. The DOS  $D(E)$  has been fitted to

$$D(E) = A_{\text{VB}}(E_{\text{VB}} - E)^{0.5} \quad (1)$$

for the valence band (VB) and

$$D(E) = A_{\text{CB}}(E - E_{\text{CB}})^{0.5} \quad (2)$$

for the conduction band (CB). As will be later discussed,  $E_{\text{VB}} = 0$  and  $E_{\text{CB}} \sim 0.4 \text{ eV}$ . Since  $m^*$  can be written as

$$m^* = \frac{\hbar^2}{m_e} \sqrt[3]{\pi^4 D(E) D'(E) / V^2}, \quad (3)$$

we obtain, by combining Eqs. (3) and (1) or (2):

$$m^* = \frac{\hbar^2}{m_e} \sqrt[3]{\pi^4 A^2 / 2V^2}, \quad (4)$$

where  $V$  is the volume of the supercell and  $A$  is either  $A_{\text{VB}}$  or  $A_{\text{CB}}$ .

## III. RESULTS AND DISCUSSION

### A. Transport as a function of temperature

Seebeck coefficient, resistivity and power factor measured as a function of temperature in the  $\text{Fe}_2\text{V}_{1+x}\text{Al}_{1-x}$  series ( $-0.1 < x < 0.1$ ) are displayed in Fig. 1. The electrical resistivity [Fig. 1(b)] goes through a maximum in the temperature range 300 – 600 K in both  $p$ -type or  $n$ -type compounds. It is a behavior typical of degenerate semiconductors entering the intrinsic regime at elevated temperature: at temperatures

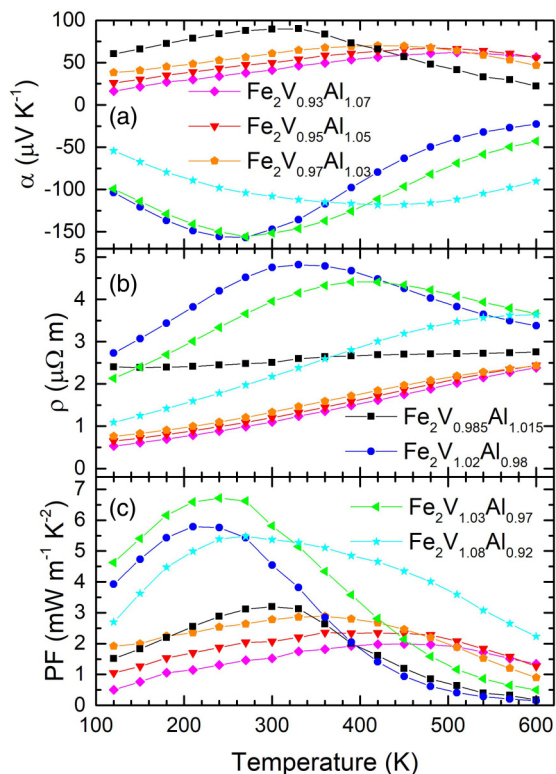


FIG. 1. (a) Seebeck coefficient ( $\alpha$ ), (b) electrical resistivity ( $\rho$ ) and (c) power factor ( $PF$ ) as a function of temperature in  $\text{Fe}_2\text{V}_{1+x}\text{Al}_{1-x}$  ( $-0.1 < x < +0.1$ ).

lower than the maximum, the numerous majority charge carriers dominate the transport which is “metal-like” whereas at temperatures larger than the maximum, both majority and minority carriers contribute to the transport, decreasing the resistivity. Similarly, the Seebeck coefficient versus temperature [Fig. 1(a)] displays in the range [270 – 520 K] a maximum or a minimum in  $p$ - or  $n$ -type  $\text{Fe}_2\text{V}_{1+x}\text{Al}_{1-x}$  compositions respectively. Again, these variations are typical of degenerate semiconductors entering the intrinsic regime at high temperature.

As already discussed in the literature [14,17], it can easily be noticed that the V-rich samples display an electron-type conduction while the Al-rich samples display a hole-type conduction. For both types, the Seebeck coefficient varies according to the sample composition: those with the compositions the closest to the stoichiometry display the largest absolute value of Seebeck coefficient, whereas the most off-stoichiometric samples display the smallest values. This is in line with the electron acceptor and donor character of  $\text{Al}_V$  and  $\text{V}_{\text{Al}}$  defects, respectively [31], which control the charge carrier concentration in these samples. The  $p$ -type off-stoichiometric samples display maximum values close to  $90 \mu\text{V K}^{-1}$ , while the  $n$ -type off-stoichiometric samples display absolute maximum values larger than  $155 \mu\text{V K}^{-1}$ . Overall, the resistivity values [Fig. 1(b)] are remarkably small: they are lower than  $\sim 5 \mu\Omega \text{ m}$  and they are even smaller than  $\sim 2 \mu\Omega \text{ m}$  in the  $p$ -type off-stoichiometric samples. This leads to maximum power factor values of  $PF = 3.2 \text{ mW m}^{-1} \text{ K}^{-2}$  at 325 K and  $PF = 6.7 \text{ mW m}^{-1} \text{ K}^{-2}$  at 250 K in the  $p$ - and  $n$ -type sam-

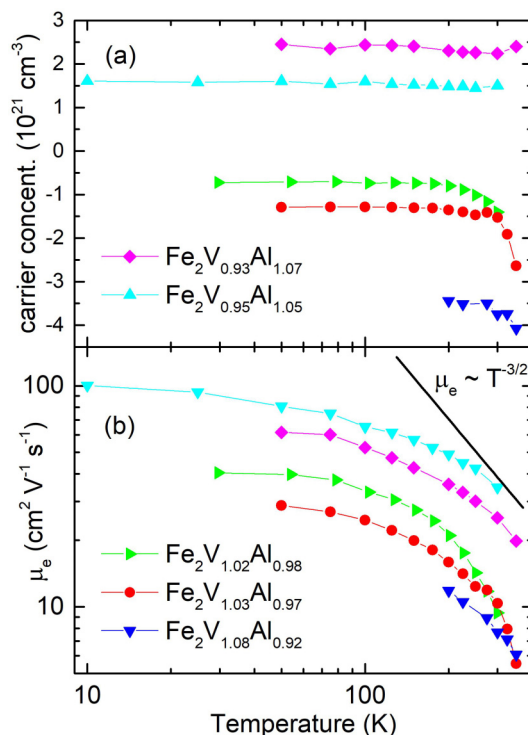


FIG. 2. (a) Charge carrier concentration and (b) Hall mobility ( $\mu_e$ ) as a function of temperature in  $\text{Fe}_2\text{V}_{1+x}\text{Al}_{1-x}$  ( $-0.1 < x < +0.1$ ).

ples, respectively [Fig. 1(c)], in agreement with the literature [17]. Nonetheless, the smaller values of the resistivity in the  $p$ -type samples do not compensate the larger Seebeck coefficient in the  $n$ -type samples. This point will be related to the differing density of states effective masses in  $p$ - and  $n$ -type  $\text{Fe}_2\text{V}_{1+x}\text{Al}_{1-x}$ .

### B. Seebeck coefficient at 220 K

To better understand the origin of these asymmetrical performances, we investigated the valence and conduction density of states effective mass ( $m^*$ ) by combining Seebeck coefficient and charge carrier concentration data in a single parabolic band model. Prior to this modeling, it is necessary to determine the energy dependence of the relaxation time by plotting the electronic mobility ( $\mu_e$ ) as a function of temperature. As can be noticed in Fig. 2(b),  $\mu_e$  is systematically larger in  $p$ -type compositions than in  $n$ -type compositions: this point will be further discussed. Between 10 and 50 K,  $\mu_e$  weakly depends on temperature for both conduction types, as expected in the case of holes / electrons predominantly scattered by impurities in a degenerate semiconductor [32,33]. In this last temperature range, the electronic relaxation time does not depend on energy and can be described by the following equation (Ref. [32]):

$$\tau_i = \frac{\tau_i^0}{c_i}, \quad (5)$$

where  $c_i$  is the impurity concentration in mol / mol  $\text{Fe}_2\text{VAl}$  and  $\tau_i^0$  is a time coefficient in seconds, describing the relaxation time dependence on the impurity concentration. In the

200 – 300 K temperature range for *n*-type samples and above 250 K for the *p*-type samples,  $\mu_e$  displays the well-known  $T^{-3/2}$  behavior, characteristic of charge carriers predominantly scattered by acoustic phonons [34]. The relaxation time ( $\tau$ ) dependence on the energy ( $\varepsilon$ ) is hence well described for *n*- and for *p*-type conduction in these previously mentioned temperature ranges by the following relation [32,34]:

$$\tau_p = \tau_p^0 \varepsilon^{-1/2}. \quad (6)$$

For *p*-type samples between 200 and 250 K,  $\mu_e$  displays a thermal behavior intermediate between  $T^0$  and  $T^{-3/2}$ , characteristic of hole scattering by both the impurities and acoustic phonons. In this case, the electronic relaxation time is a Matthiessen combination of the two scattering processes:

$$\frac{1}{\tau} = \frac{1}{\tau_i} + \frac{1}{\tau_p} \quad (7)$$

It is incorrect to implement a single parabolic band model at 300 K for these compounds because some of them are already in the intrinsic regime, with two kinds of carriers contributing to the electronic transport at this temperature [Figs. 1(a) and 1(b)]. A better temperature to implement such a simple model in this  $\text{Fe}_2\text{V}_{1+x}\text{Al}_{1-x}$  series is a lower temperature. Indeed, transport dominated by a single type of carriers is confirmed for several samples with ( $-0.1 < x < 0.1$ ) in the [10; 250 K] temperature range by the temperature-independent character of the charge carrier concentration displayed in Fig. 2(a). Similarly, Seebeck coefficient versus temperature [Fig. 1(a)] shows no slope change that would have been characteristic of bipolar transport in the [120–270 K] temperature range, for none of the samples. We hence chose  $T = 220$  K to implement a single-band model because at this temperature, a single type of carrier dominates the electronic transport for both types of conduction.

For *n*-type compositions at  $T = 220$  K, electrons are predominantly scattered by [34,35] the phonons. Seebeck coefficient ( $\alpha$ ), the electron density ( $n$ ), the electrical conductivity ( $\sigma$ ) and the electronic mobility ( $\mu_e$ ) are thus related to the reduced chemical potential ( $\eta = \frac{\mu}{k_B T}$ ) by the following equations [35]:

$$\alpha_n = -\frac{k_B}{e} \left( 2 \frac{F_1(\eta)}{F_0(\eta)} - \eta \right), \quad (8)$$

$$n \text{ or } p = 4\pi \left( \frac{2m^* k_B T}{h^2} \right)^{\frac{3}{2}} F_{\frac{1}{2}}(\eta), \quad (9)$$

$$\sigma = \frac{8\pi e^2 \tau_p^0(T)}{3} \left( \frac{2}{h^2} \right)^{\frac{3}{2}} (m^*)^{\frac{1}{2}} k_B T F_0(\eta), \quad (10)$$

$$\mu_e = \frac{2e\tau_p^0(T)}{3m^*(k_B T)^{1/2}} \frac{F_0(\eta)}{F_{\frac{1}{2}}(\eta)}, \quad (11)$$

where the  $F_q$  are Fermi integrals,  $k_B$  the Boltzmann's constant,  $e$  the elementary charge,  $h$  the Planck's constant. The Fermi integrals are defined by the expression:

$$F_q(\eta) = \int_0^\infty \frac{x^q}{[1 + e^{(x-\eta)}]} dx, \quad (12)$$

where  $x = \frac{\varepsilon}{k_B T}$  is the reduced energy.

For *p*-type compositions at 220 K, both impurities and phonons scatter the holes. The Seebeck coefficient is thus

given by the following expression [36]:

$$\alpha_p = \frac{\int_0^\infty (\varepsilon - \mu) \varepsilon^{3/2} \tau(\varepsilon) \left( -\frac{\partial f_0}{\partial \varepsilon} \right) d\varepsilon}{eT \int_0^\infty \varepsilon^{3/2} \tau(\varepsilon) \left( -\frac{\partial f_0}{\partial \varepsilon} \right) d\varepsilon} \quad (13)$$

After some algebra, it can be transformed into

$$\alpha_p = \frac{k_B}{e} \left( \frac{G_{5/2}(\eta)}{G_{3/2}(\eta)} - \eta \right), \quad (14)$$

where  $G_q$  are integrals defined by

$$G_q(\eta) = \int_0^\infty \frac{x^q e^{(x-\eta)}}{[1 + e^{(x-\eta)}]^2 \left[ \frac{c_i}{\tau_i^0} + \frac{(k_B T)^{1/2} x^{1/2}}{\tau_p^0} \right]} dx. \quad (15)$$

At 10 K, as already stated, electrons or holes are predominantly scattered by the impurities and the mobility can be expressed as  $\mu_e = \frac{e\tau_i^0}{m^*c_i}$  [35]. A linear fit to  $1/\mu_e$  (values extracted from Fig. 2) versus  $c_i = x(\text{Al})$  (plot not shown) yields  $\frac{e\tau_i^0}{m^*} = 4.85 \text{ cm}^2 \text{ V}^{-1} \text{ s}^{-1}$  and a reliability factor of 0.998, validating Eq. (5). At high temperature, electrons are predominantly scattered by the phonons and the mobility is given by Eq. (11). Taking the ratio of mobility at 10 K and temperature  $T$  eliminates  $m^*$  and leads to

$$\frac{\mu_e(10 \text{ K})}{\mu_e(T)} = \frac{3\tau_i^0 (k_B T)^{1/2} F_{\frac{1}{2}}(\eta)}{2c_i \tau_p^0(T) F_0(\eta)} \quad (16)$$

and to

$$R(T, \eta) = \frac{c_i \tau_p^0(T)}{\tau_i^0 (k_B T)^{1/2}} = \frac{3\mu_e(T) F_{1/2}(\eta)}{2\mu_e(10 \text{ K}) F_0(\eta)}. \quad (17)$$

Equation (17) can be used to approximate  $R(T, \eta)$  at 220 K by the expression

$$R(220 \text{ K}, \eta) \approx \frac{3\mu_e(220 \text{ K}) F_{\frac{1}{2}}(\eta)}{2\mu_e(10 \text{ K}) F_0(\eta)}. \quad (18)$$

Substituting Eq. (18) in Eqs. (14) and (15) gives

$$\alpha_p(220 \text{ K}) \approx \frac{k_B}{e} \left( \frac{H_{5/2}(\eta)}{H_{3/2}(\eta)} - \eta \right) \quad (19)$$

with

$$H_q(\eta) = \int_0^\infty \frac{x^q e^{(x-\eta)}}{[1 + e^{(x-\eta)}]^2 \left[ \frac{3\mu_e(220 \text{ K})}{2\mu_e(10 \text{ K})} \frac{F_{\frac{1}{2}}(\eta)x^{\frac{1}{2}}}{F_0(\eta)} \right]} dx. \quad (20)$$

For both  $\text{Fe}_2\text{V}_{0.93}\text{Al}_{1.07}$  and  $\text{Fe}_2\text{V}_{0.95}\text{Al}_{1.05}$  displayed in Fig. 2(b),  $\frac{\mu_e(220 \text{ K})}{\mu_e(10 \text{ K})} = 0.48$  experimentally.

Using the same formalism for  $\sigma$  and  $\mu_e$  leads to

$$\sigma = \frac{8\pi e^2 \tau_p^0(T)}{3} \left( \frac{2}{h^2} \right)^{\frac{3}{2}} (m^*)^{\frac{1}{2}} k_B T H_{3/2}(\eta), \quad (21)$$

$$\mu_e = \frac{2e\tau_p^0(T)}{3m^*(k_B T)^{1/2}} \frac{H_{3/2}(\eta)}{F_{\frac{1}{2}}(\eta)}. \quad (22)$$

For *p*-type and *n*-type conduction, a value of the density of states effective mass can be derived from a fit of Eqs. (9) and (19) and (9) and (8), respectively, to a plot of the experimental Seebeck coefficient versus charge carrier's density data (the so-called Ioffe-Pisarenko plot) as shown in Figs. 3(a) and 4(a). Not only the data (gathered in Table I) for the *p*- and *n*-type  $\text{Fe}_2\text{V}_{1+x}\text{Al}_{1-x}$  compositions are plotted but also those

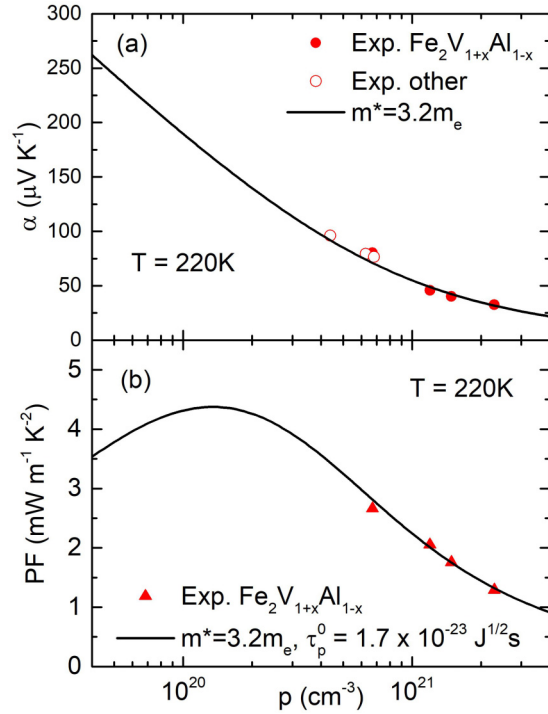


FIG. 3. (a) Seebeck coefficient ( $\alpha$ ) as a function of the hole concentration, at 220 K. Red solid circles: experimental data for  $\text{Fe}_2\text{V}_{1-x}\text{Al}_{1+x}$  ( $x > 0.0$ ); red open circles: experimental data for  $\text{Fe}_{2.08}\text{V}_{0.92}\text{Al}$ ,  $\text{Fe}_{2.04}\text{V}_{0.96}\text{Al}$  and  $\text{Fe}_{1.92}\text{VAl}_{1.08}$ ; continuous black line: fit with a single parabolic band and “two  $\tau$ ” model and an effective mass  $m^* = 3.2m_e$ . (b) Power factor ( $PF$ ) at 220 K as a function of the hole concentration. Solid symbols: experimental data; solid line: fit with single parabolic band model and an effective DOS mass  $m^* = 3.2m_e$  and a relaxation time parameter  $\tau_p^0 = 1.7 \times 10^{-23} \text{ J}^{1/2} \text{ s}$ .

for some compositions of the  $\text{Fe}_{2-x}\text{V}_{1+x}\text{Al}$  and  $\text{Fe}_{2+x}\text{VAl}_{1-x}$  series (see Table II) since  $\text{Fe}_V(\text{V}_{\text{Fe}})$  and  $\text{Al}_{\text{Fe}}(\text{Fe}_{\text{Al}})$  are electron acceptor (donor) antisite defects, as well as  $n$ -type  $\text{Fe}_2\text{VAl}_{0.9}\text{Si}_{0.1}$  and  $\text{Fe}_2\text{V}_{0.95}\text{Ta}_{0.05}\text{Al}_{0.9}\text{Si}_{0.1}$  extracted from Ref. [13]. Other compositions reported in Ref. [14] were discarded because their Hall coefficient changed sign in the 100 – 300 K temperature range, evidencing the dual nature of their carriers.

On the one hand, an initial fit (not shown) of the less accurate “single  $\tau$ ” model [Eq. (8)] yielded  $m^* = 3.7m_e \pm 0.3m_e$ . ( $m_e$  is the bare electron mass) for the  $p$ -type samples ( $\text{Fe}_2\text{V}_{1+x}\text{Al}_{1-x}$   $x < 0.0$ ,  $\text{Fe}_{2.08}\text{V}_{0.92}\text{Al}$ ,  $\text{Fe}_{2.04}\text{V}_{0.96}\text{Al}$  and

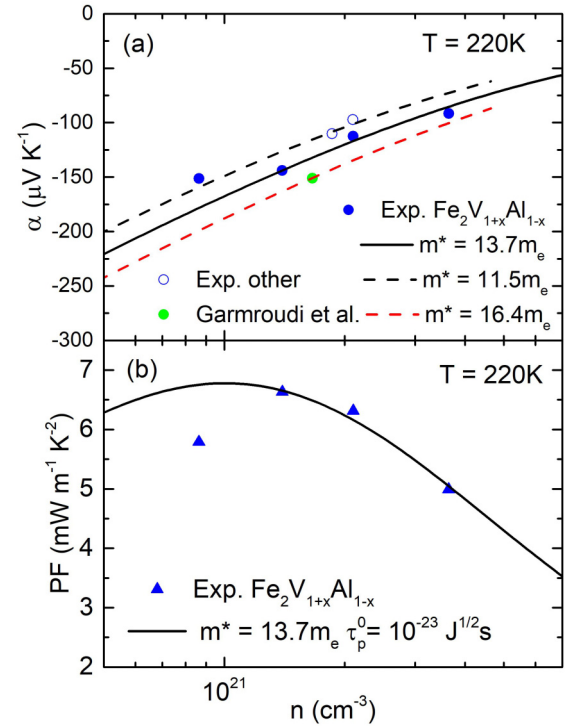


FIG. 4. (a) Seebeck coefficient ( $\alpha$ ) as a function of the electron concentration, at 220 K. Blue solid circles: experimental data for  $\text{Fe}_2\text{V}_{1+x}\text{Al}_{1-x}$  ( $x > 0.0$ ); blue open circles: experimental data for  $\text{Fe}_2\text{VAl}_{0.9}\text{Si}_{0.1}$  (Ref. [13]) and  $\text{Fe}_{2.08}\text{VAl}_{0.92}$ ; green solid circle: experimental data for  $\text{Fe}_2\text{V}_{0.95}\text{Ta}_{0.05}\text{Al}_{0.9}\text{Si}_{0.1}$  (Ref. [13]); lines: fits with a single parabolic band model and an effective DOS mass  $m^* = 11.5m_e$  (dashed black),  $m^* = 13.7m_e$  (continuous black) and  $m^* = 16.4m_e$  (dashed red line). (b) Power factor ( $PF$ ) at 220 K as a function of the hole concentration. Solid symbols: experimental data; solid line: fit with a single parabolic band model, an effective mass  $m^* = 13.7m_e$  and a relaxation time parameter  $\tau_p^0 = 1.0 \times 10^{-23} \text{ J}^{1/2} \text{ s}$ .

$\text{Fe}_{1.92}\text{VAl}_{1.08}$ ). Nonetheless, as previously discussed,  $p$ -type samples are more rigorously represented by a  $m^* = 3.2m_e \pm 0.3m_e$  theoretical curve derived from the “two  $\tau$ ” model [Eq. (19)], regardless of the nature of their off-stoichiometry [Fig. 3(a)]. This last value is significantly smaller than the  $m^* = 4.7m_e$  value derived by Anand *et al.* [15] based on assumed values of hole concentrations. On the other hand, the  $n$ -type samples [Fig. 4(a)] cannot be represented by a single density of states effective mass. The  $n$ -type  $\text{Fe}_2\text{V}_{1+x}\text{Al}_{1-x}$

TABLE I. Electronic transport coefficients measured at 220 K in  $\text{Fe}_2\text{V}_{1+x}\text{Al}_{1-x}$  ( $-0.1 < x < +0.1$ ). Hole concentrations are positive whereas electron concentrations are negative.

Compositions	$p/n$ ( $10^{20} \text{ cm}^{-3}$ )	$\alpha$ ( $\mu\text{V K}^{-1}$ )	$\sigma$ ( $\text{S m}^{-1}$ )	$PF$ ( $\text{mW m}^{-1} \text{K}^{-2}$ )	$\mu_e$ ( $\text{cm}^2 \text{V}^{-1} \text{s}^{-1}$ )
$\text{Fe}_2\text{V}_{0.93}\text{Al}_{1.07}$	23	32.5	$12.2 \cdot 10^5$	1.3	33.4
$\text{Fe}_2\text{V}_{0.95}\text{Al}_{1.05}$	15	40.1	$10.8 \cdot 10^5$	1.8	45.6
$\text{Fe}_2\text{V}_{0.97}\text{Al}_{1.03}$	12	45.8	$9.7 \cdot 10^5$	2.1	50.6
$\text{Fe}_2\text{V}_{0.985}\text{Al}_{1.015}$	6.7	80.4	$4.1 \cdot 10^5$	2.7	38.4
$\text{Fe}_2\text{V}_{1.02}\text{Al}_{0.98}$	-8.6	-151.2	$2.5 \cdot 10^5$	5.8	18.3
$\text{Fe}_2\text{V}_{1.03}\text{Al}_{0.97}$	-14	-143.9	$3.2 \cdot 10^5$	6.6	14.3
$\text{Fe}_2\text{V}_{1.08}\text{Al}_{0.92}$	-36	-91.8	$6.03 \cdot 10^5$	5.0	10

TABLE II. Charge carrier concentration, Seebeck coefficient and Hall mobility at 220 K in chosen  $\text{Fe}_{2-x}\text{V}_{1+x}\text{Al}$  and  $\text{Fe}_{2+x}\text{VAl}_{1-x}$  compositions, in  $\text{Fe}_2\text{VAl}_{0.9}\text{Si}_{0.1}$  and  $\text{Fe}_2\text{V}_{0.95}\text{Ta}_{0.05}\text{Al}_{0.9}\text{Si}_{0.1}$ . The data for these two last composition are extracted from Ref. [13]

Compositions	$p/n$ ( $10^{20} \text{ cm}^{-3}$ )	$\alpha$ ( $\mu\text{V K}^{-1}$ )	$\mu_e$ ( $\text{cm}^2 \text{ V}^{-1} \text{ s}^{-1}$ )
$\text{Fe}_{2.04}\text{V}_{0.96}\text{Al}$	4.4	96.2	23.3
$\text{Fe}_{2.08}\text{V}_{0.92}\text{Al}$	6.3	79.2	12.7
$\text{Fe}_{1.92}\text{VAl}_{1.08}$	6.8	76.4	8.0
$\text{Fe}_{2.08}\text{VAl}_{0.92}$	-18.6	-110.1	3.9
$\text{Fe}_2\text{VAl}_{0.9}\text{Si}_{0.1}$	-21.0	-97.3	19.2
$\text{Fe}_2\text{V}_{0.95}\text{Ta}_{0.05}\text{Al}_{0.9}\text{Si}_{0.1}$	-16.6	-151	16.0

$x = 0.03$  and  $0.05$  samples are well represented by a  $m^* = 13.7m_e \pm 0.3m_e$  theoretical curve whereas the  $\text{Fe}_2\text{V}_{1.02}\text{Al}_{0.98}$ ,  $\text{Fe}_{2.08}\text{VAl}_{0.92}$  and  $\text{Fe}_2\text{VAl}_{0.9}\text{Si}_{0.1}$  samples are represented by  $m^* = 11.5m_e \pm 0.3m_e$ , a value significantly smaller. This implies that the effective mass increases with the electron concentration and that probably,  $\text{V}_{\text{Al}}$  defects also increase the effective mass. This qualitatively agrees with past DFT calculations [31] and to photoemission spectroscopy experiments [37], which indicated that  $\text{V}_{\text{Al}}$  defects increase the band gap and modify the relative position of the conduction bands. This increase of the effective mass upon  $\text{V}_{\text{Al}}$  self-doping thus probably arises from relative band displacements or “band convergence”. This scenario has also been invoked in Ref. [13] to explain the increase of power factor in  $\text{Fe}_2\text{V}_{1-x}\text{Ta}_x\text{Al}_{1-y}\text{Si}_y$ . An effective mass  $m^* = 16.4m_e \pm 0.3m_e$ , even larger than in  $\text{Fe}_2\text{V}_{1+x}\text{Al}_{1-x}$ , can be estimated from the  $\text{Fe}_2\text{V}_{0.95}\text{Ta}_{0.05}\text{Al}_{0.9}\text{Si}_{0.1}$  datum extracted from the former reference, confirming a change in the structure of the conduction bands in  $\text{Fe}_2\text{V}_{1-x}\text{Ta}_x\text{Al}_{1-y}\text{Si}_y$  upon Ta substitution.

These values of conduction band effective mass are larger than what is commonly observed in typical thermoelectric materials ( $m^* = 3.2m_e$  for  $n$ -type  $\text{CoSb}_3$  [38,39] or  $m^* = 2.9m_e$  for  $\text{ZrNiSn}$  [40]) but it is not so unusual since  $m^* = 10m_e$  was reported in the  $p$ -type half-Heusler alloy  $\text{FeNbSb}$  [41]. It also agrees well with the value  $m^* = 12.8m_e$  derived in Refs. [15,16] and to a lesser extent with  $m^* = 10m_e$  reported in Ref. [13] for the  $\text{Fe}_2\text{VAl}$  CBs. It is thus noteworthy that the effective mass depends on the nature of the dopant in  $n$ -type  $\text{Fe}_2\text{VAl}$ , whereas  $p$ -type  $\text{Fe}_2\text{VAl}$  seems to be less sensitive. Finally, the plots of Seebeck coefficient versus valence electron count found in various references [15,42] for various dopants have often been considered as generic for  $\text{Fe}_2\text{VAl}$ . This assertion should be revised for the  $n$ -type portion of these plots, given the dependence of the effective mass with the nature of the dopants in the CB.

As mentioned in Sec. II, we tried to corroborate these experimental effective masses with DFT calculations. The results for the Al-rich or  $p$ -type compound are reported in Figs. 5(a) and 6(a), where the DOS and band structure calculated for  $\text{Fe}_2\text{V}_{0.96}\text{Al}_{1.04}$  are plotted. Close to the Fermi energy ( $E_F$ ) the DOS arising from the V  $3d$  ( $e_g$ ) dominated conduction band which crosses  $E_F$  around the X point, is small compared to the DOS arising from the two Fe valence

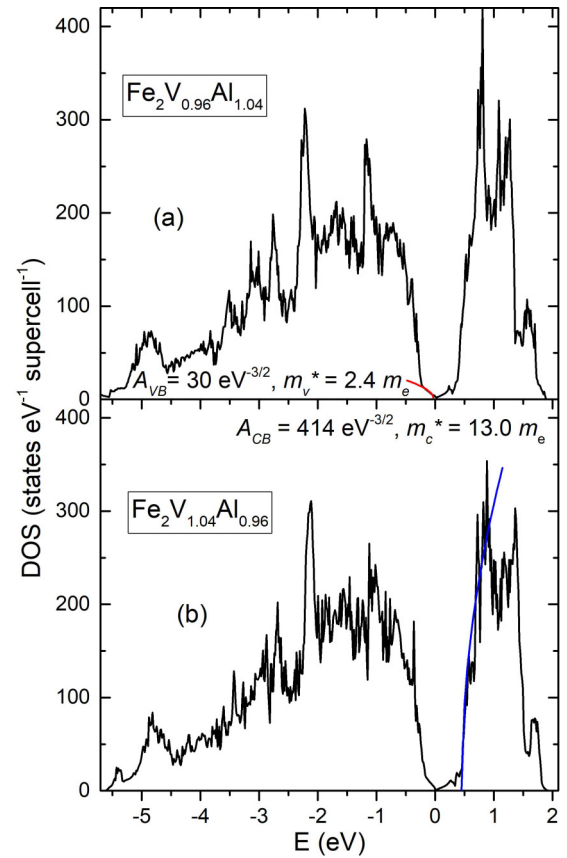


FIG. 5. DFT-calculated density of states (DOS) as a function of energy ( $E$ ) in  $\text{Fe}_2\text{V}_{0.96}\text{Al}_{1.04}$  (a) and in  $\text{Fe}_2\text{V}_{1.04}\text{Al}_{0.96}$  (b). The red and blue lines are fits with a parabolic DOS (see text) to the DFT results for the Al-rich and V-rich composition, respectively.

bands ( $3d t_{2g} - 4p$  mixture), which cross the Fermi energy around the  $\Gamma$ -point in the Brillouin zone. Indeed, after fitting parabolic DOS to the valence and conduction bands and integrating from their edges to the Fermi energy leads to  $0.05 \pm 0.01$  holes / supercell and to  $0.04 \pm 0.01$  electrons / supercell, respectively. This slight imbalance in the number of holes and electrons combined with the larger hole mobility leads to  $\text{Fe}_2\text{V}_{0.96}\text{Al}_{1.04}$  being  $p$  type. At  $E - E_F \sim 0.4$  eV, the conduction DOS steeply increases due to nondispersing Fe  $3d$ -bands (nonbonding  $e_g$ ) whereas the valence DOS also increases at  $E - E_F \sim -0.25$  eV because of a less dispersing Fe  $3d$ -band ( $t_{2g}$ ), which peaks at the X point. The valence DOS in Fig. 5(a) is fitted to Eq. (1). The experimental hole concentration of  $1.5 \times 10^{21} \text{ cm}^{-3}$  (Table I) leads to an energy region for the fit of the valence band directly below the Fermi energy ( $E_F$ ) and this fit gives a value of  $A_{vb}$  equal to  $30 \text{ eV}^{-3/2}$ . This results in an effective mass for the  $p$ -type compound of  $2.4m_e$ , which differs slightly from the experimental value ( $3.2m_e$ ). This small discrepancy could arise from two different reasons: (i) an inaccurate calculation of the dispersion of the two Fe valence bands culminating slightly above  $E_F$  at  $\Gamma$  in Fig. 6; (ii) a misestimation of the calculated position of the less dispersing bands ( $\sim -0.2 - 0.3$  eV below the Fermi energy) (Fig. 6). In assumption (ii), the contribution of the bands to the transport would increase with increasing hole concentration. This would lead to an increase of the

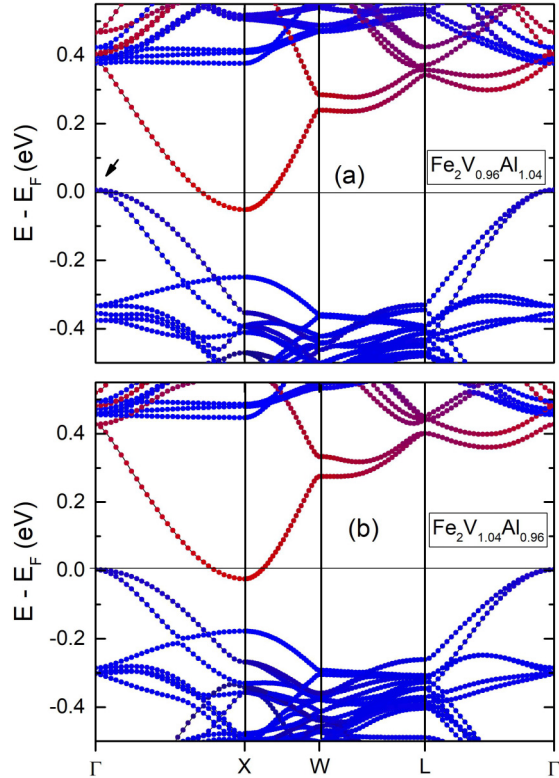


FIG. 6. Panel (a) band structure of  $\text{Fe}_2\text{V}_{0.96}\text{Al}_{1.04}$ , the arrow indicates the two hole pockets at  $\Gamma$ . (b) band structure of  $\text{Fe}_2\text{V}_{1.04}\text{Al}_{0.96}$ . In both panels, the RedGreenBlue (RGB) index of the color (RGB color model, Ref. [50]) of the closed circle is generated by adding the weighted atomic contribution to the band. 100% Fe is “bright blue” (0,0,255), 100% V is “bright red” (255,0,0) and 100% Al is “bright green” (0,255,0). Purple bands correspond to nearly 50% Fe + 50% V; dark blue bands correspond to approximately 80% Fe + 15% V + 5% Al. There is no green symbol due to the weak Al contribution at these energies.

effective mass with this last parameter. However, a slight decrease is noticeable in Fig. 3(a), which is compatible with calculations of the DOS effective mass in  $\text{Fe}_2\text{V}_{0.93}\text{Al}_{1.07}$  with a larger concentration of holes (exp.  $p = 2.3 \times 10^{21} \text{ cm}^{-3}$ ):  $m_v^* = 2.0m_e$ . Assumption (i), e.g., inaccurate calculated dispersion is thus the most probable explanation for the slight effective mass discrepancy. It also suggests that the less dispersing bands ( $\sim -0.2$  eV below the Fermi energy) do not take part in the electronic transport of these  $p$ -type  $\text{Fe}_2\text{V}_{1+x}\text{Al}_{1-x}$  compositions.

The results for the V-rich or  $n$ -type compound are reported in Figs. 5(b) and 6(b). Compared to  $p$ -type  $\text{Fe}_2\text{V}_{0.96}\text{Al}_{1.04}$ , the DOS in  $n$ -type  $\text{Fe}_2\text{V}_{1.04}\text{Al}_{0.96}$  weakly changes [Fig. 5(b)]. Going more into the details by examining the band structure, the Fe-valence bands do not cross anymore the Fermi energy whereas the conduction bands (V 3d- $e_g$  and Fe 3d- $e_g$ ) are slightly shifted upward, in agreement with Ref. [28]. We adjusted the energy region of the fit to the experimental charge carrier concentration of  $1.5 \times 10^{21} \text{ cm}^{-3}$  (Table I), e.g. for  $E - E_F \geq 0.4$  eV where the DOS steeply increases, leading to  $E_{CB} = +0.4$  eV as shown in Fig. 5(b). For the same carrier concentration, the fitted VB DOS is found directly

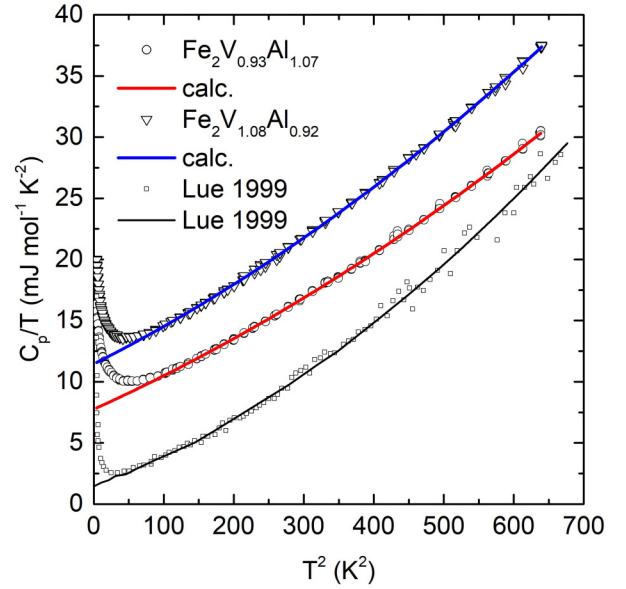


FIG. 7. Specific heat ( $C_p$ ) divided by  $T$  plotted as a function of  $T^2$  for  $\text{Fe}_2\text{V}_{0.93}\text{Al}_{1.07}$  and  $\text{Fe}_2\text{V}_{1.08}\text{Al}_{0.92}$ . Open triangles and circles: our measured values. Continuous lines: fit with the equation  $C_p = \gamma T + \beta T^3 + \delta T^5$  of the present measurements. Open squares and black line: measurements extracted from Lue *et al.* [45].

below  $E_F = E_{VB} = 0$  eV. This difference arises because the VB DOS is larger than the CB DOS in the close vicinity of  $E_F$  (Fig. 5). The value fitted for  $A_{CB}$  is  $414 \text{ eV}^{-3/2}$  [Eq. (2)], which yields a value of  $m^*$  equal to  $13m_e$  [Eq. (4)], in very good agreement with the experimental results. This high value of the effective mass for the  $n$ -type compound can be traced back to the flat Fe-bands (Fe  $e_g$  character) that can be seen at 0.4 eV in the band structure displayed in Fig. 6. The DOS effective mass has also been calculated in  $\text{Fe}_2\text{V}_{1.07}\text{Al}_{0.93}$  with a larger electron concentration (exp.  $N = 3.6 \times 10^{21} \text{ cm}^{-3}$ ): a larger value  $m_v^* = 14.2m_e$  was obtained. This slight increase for the calculated electron mass indeed agrees with the experimental data, which points towards an increase of the effective mass with both electrons and  $\text{V}_{\text{Al}}$  defects concentrations.

### C. Specific heat

Since the Seebeck coefficient is a measure of the entropy per charge carrier in a conductor [43], it is related to the electronic specific heat. They are both related to the density of states at the Fermi energy and in the “effective mass picture” already implemented for the Seebeck coefficient, the specific heat also depends on the effective mass [44]. It can be derived from the Sommerfeld coefficient ( $\gamma$ ) of the electronic contribution ( $\gamma T$ ) to the specific heat at constant volume, very well approximated in a solid by the specific heat at constant pressure ( $C_p$ ), more easily measured. Usually,  $C_p$  is approximated by the classical relation [44]:

$$C_p = \gamma T + \beta T^3, \quad (23)$$

where the second term arises from the phonon contribution.  $\beta$  is related to the Debye temperature ( $\theta_D$ ) by  $\theta_D = (\frac{234R}{\beta})^{1/3}$ . Both  $\gamma$  and  $\beta$  can thus be determined by a plot of  $C_p(T)/T$  versus  $T^2$  as shown in Fig. 7 for the  $p$ -type  $\text{Fe}_2\text{V}_{0.92}\text{Al}_{1.08}$

TABLE III. Values of the coefficients of the equation  $C_p = \gamma T + \beta T^3 + \delta T^5$  fitted to the measurements displayed in Fig. 5.

Compositions	$\gamma$ (mJ/mol <sup>-1</sup> K <sup>-2</sup> )	$\beta$ (mJ/mol <sup>-1</sup> K <sup>-4</sup> )	$\theta_D$ (K)	$\delta$ (mJ/mol <sup>-1</sup> K <sup>-6</sup> )
<i>p</i> -type Fe <sub>2</sub> V <sub>0.92</sub> Al <sub>1.08</sub>	7.8	0.026	406	$1.48 \times 10^{-5}$
<i>n</i> -type Fe <sub>2</sub> V <sub>1.07</sub> Al <sub>0.93</sub>	11.5	0.029	421	$1.81 \times 10^{-5}$

and *n*-type Fe<sub>2</sub>V<sub>1.07</sub>Al<sub>0.93</sub> samples. In both samples below 7 K,  $C_p(T)/T$  shows an upturn, which is, as can be noticed in Fig. 7, very similar to the one previously observed in Fe<sub>2</sub>VAl (Ref. [45]). In the previous reference, it has been ascribed to a magnetic contribution, most probably arising from magnetic defects, and modeled by a two-level Schottky anomaly. In Fig. 7, for temperatures larger than  $T^2 \sim 64$  K or  $T \geq 8$  K it is negligible, and the specific heat can hence be modeled by the equation given in Ref. [45]:

$$C_p = \gamma T + \beta T^3 + \delta T^5, \quad (24)$$

which is more accurate than Eq. (23) since it incorporates a  $T^5$  term that is a correction to the main  $T^3$  phonon contribution. The fits to the data displayed in Fig. 7 yield the values compiled in Table III. On the one hand, the fitted Debye temperatures are both close to the value  $\theta_D = 450$  K reported in Ref. [45] for Fe<sub>2</sub>VAl. On the other hand, the fitted Sommerfeld coefficients are significantly larger in the present off-stoichiometric samples than in pristine Fe<sub>2</sub>VAl ( $\gamma = 1.5$  mJ mol<sup>-1</sup> K<sup>-2</sup>) [45], reflecting the larger charge carrier concentration. A larger  $\gamma$  value is found in the *n*-type composition (11.5 mJ mol<sup>-1</sup> K<sup>-2</sup>) than in the *p*-type one (7.8 mJ mol<sup>-1</sup> K<sup>-2</sup>). But it cannot be concluded straightforwardly that the effective mass is larger in *n*-type Fe<sub>2</sub>V<sub>1.07</sub>Al<sub>0.93</sub> since  $D(E_F)$  not only depends on the effective mass but also on the position of the Fermi energy  $E_F$  in the band. The Sommerfeld coefficient is indeed related [46,47] to the density of states by the equation:

$$\gamma = (1 + \lambda) \frac{\pi^2}{3} k_B^2 D(E_F), \quad (25)$$

where  $\lambda$  is the electron-phonon and / or electron - electron interaction parameter. Assuming that the electron-phonon and / or electron - electron interaction parameter is the same in both *n*-type and *p*-type samples, the ratio of Sommerfeld coefficients  $\frac{\gamma_n}{\gamma_p}$  is given by the simple expression  $\frac{\gamma_n}{\gamma_p} = \frac{D_n(E_{F_n})}{D_p(E_{F_p})}$ , where  $D_p$  and  $D_n$  are the densities of states and  $E_{F_p}$  and  $E_{F_n}$  are the positions of the Fermi energy in *p*-type Fe<sub>2</sub>V<sub>0.92</sub>Al<sub>1.08</sub> and *n*-type Fe<sub>2</sub>V<sub>1.07</sub>Al<sub>0.93</sub> respectively. Both these quantities can be estimated from the DOS calculated by DFT in Fe<sub>2</sub>V<sub>0.96</sub>Al<sub>1.04</sub> and Fe<sub>2</sub>V<sub>1.04</sub>Al<sub>0.96</sub> (Fig. 5). By integrating the DOS up to the energy  $E$  and dividing by the supercell volume ( $V_{sc} = 1250.05 \text{ \AA}^3$ ), one obtains the number of charge carriers per unit of volume at 0 K with an energy smaller than  $E$  ( $N(E)$ ). Since the Hall charge carrier concentrations measured below 220 K does not depend on temperature,  $N(E)$  can be equated to these concentrations in *p*-type Fe<sub>2</sub>V<sub>0.92</sub>Al<sub>1.08</sub> and *n*-type Fe<sub>2</sub>V<sub>1.07</sub>Al<sub>0.93</sub> ( $p = 2.2 \times 10^{21} \text{ cm}^{-3}$  and  $n = 3.6 \times 10^{21} \text{ cm}^{-3}$ , respectively) and the corresponding Fermi energies  $E_{F_p}$ ,  $E_{F_n}$  and densities of states  $D_p(E_{F_p})$  and  $D_n(E_{F_n})$  can thus be derived. In *p*-type Fe<sub>2</sub>V<sub>0.92</sub>Al<sub>1.08</sub>,  $E_{F_p} = -0.26 \pm 0.02$  eV, being in the DOS region where  $m_v^* = 2.4m_e$  and  $D_p(E_{F_p}) = 27 \pm$

5 states eV<sup>-1</sup>supercell<sup>-1</sup>. In *n*-type Fe<sub>2</sub>V<sub>1.07</sub>Al<sub>0.93</sub>,  $E_{F_n} = +0.47 \pm 0.02$  eV is in the DOS region where  $m_c^* = 13.0m_e$  and  $D_n(E_{F_n}) = 52 \pm 5$  states eV<sup>-1</sup>supercell<sup>-1</sup>, leading to  $\frac{D_n(E_{F_n})}{D_p(E_{F_p})} = 1.9 \pm 0.5$ , in fair agreement with the experimental value of 1.5 for  $\frac{\gamma_n}{\gamma_p}$ . This calculation strongly suggests that  $\gamma_n > \gamma_p$  does not arise from the relative position of the Fermi energy in the *n*- and *p*-type samples but from the DOS and effective mass being larger in *n*- than in *p*-type Fe<sub>2</sub>VAl, in agreement with the transport measurements.

#### D. Electronic mobility and power factor at 220 K

The values of  $m^*$  are now used to calculate the electrical conductivity [Eq. (10)] and power factor  $PF = \alpha^2 \sigma$  at 220 K for both type of conduction in the entire range of hole and electron densities. The samples from the other Fe<sub>2+x</sub>V<sub>1-x</sub>Al and Fe<sub>2+x</sub>VAl<sub>1-x</sub> series, which had been previously used in the Ioffe - Pisarenko plots [Figs. 3(a) and 4(a)] were discarded because, as already noticed in Ref. [14], they display electronic mobility values smaller than the main Fe<sub>2</sub>V<sub>1+x</sub>Al<sub>1-x</sub> series. In the former reference, this difference in electronic mobility between series has been ascribed to electron scattering by magnetic and / or new in-gap states arising from antisite defects (Fe<sub>V</sub> or Fe<sub>Al</sub> for instance). In *p*-type Fe<sub>2</sub>VAl, to adjust the calculations to  $\mu_e = 33.4 \text{ cm}^2 \text{ V}^{-1} \text{ s}^{-1}$  when  $p = 2.3 \times 10^{21} \text{ cm}^{-3}$ , the experimental value of electronic mobility found in Fe<sub>2</sub>V<sub>0.97</sub>Al<sub>1.03</sub>, the parameter  $\tau_p^0$  was set to the value  $\tau_p^0 = 1.7 \times 10^{-23} \text{ J}^{1/2} \text{ s}$ . The calculated and experimental power factors are presented in Fig. 3(b), highlighting a good agreement between them. A noticeable maximum  $PF_{\max} = 4.4 \text{ mW m}^{-1} \text{ K}^{-2}$  at 220 K would be reached if the hole density were  $p_{\text{opt}} = 1.3 \pm 0.3 \times 10^{20} \text{ cm}^{-3}$ . Fe<sub>2</sub>V<sub>0.985</sub>Al<sub>1.015</sub> is our best *p*-type sample, which displays  $PF_{\max} = 2.7 \text{ mW m}^{-1} \text{ K}^{-2}$  for  $p = 6.7 \times 10^{20} \text{ holes cm}^{-3}$  whereas a similar value of  $2.5 \text{ mW m}^{-1} \text{ K}^{-2}$  at 220 K is reported in the literature in *p*-type Fe<sub>2</sub>V<sub>0.97</sub>Al<sub>1.03</sub> [17]. The optimization of  $PF$  in *p*-type Fe<sub>2</sub>VAl is thus difficult and has not yet been achieved, despite larger values of electronic mobility for this conduction type (Table I). This is due to the occurrence of intrinsic defects such as pairs of Al<sub>V</sub> and V<sub>Al</sub> defects [29]. These electron acceptors and donors respectively, can easily produce in stoichiometric Fe<sub>2</sub>VAl samples a hole density  $p_{\text{int}} \sim 3 \times 10^{20} \text{ holes cm}^{-3}$  at 300 K [13,48], which is twice larger than the optimum value. In *n*-type Fe<sub>2</sub>VAl, the  $PF(n)$  data shown in Fig. 4(b) are well adjusted by the  $\tau_p^0 = 1.0 \times 10^{-23} \text{ J}^{1/2} \text{ s}$  value. Before discussing the optimized  $PF$ , this last value of the relaxation time parameter permits us to calculate the ratio of the electron mobility in *p*-type and *n*-type Fe<sub>2</sub>VAl. Starting from Eqs. (11) and (22), at a fixed temperature and chemical potential, the theoretical mobility ratio (holes over electrons) is simply given by  $\frac{\mu_{ev}}{\mu_{ec}} = \frac{\tau_{pv}^0 m_c^*}{\tau_{pe}^0 m_v^*} \frac{H_{\frac{3}{2}}(\eta)}{F_0(\eta)}$ . The ratio  $\frac{H_{\frac{3}{2}}(\eta)}{F_0(\eta)}$  does not vary with  $\eta$

within the range of reduced chemical potentials (4.5 – 14) corresponding to the range of charge carrier concentrations reported in Table I ( $6.7 \times 10^{20}$ – $3.6 \times 10^{21}$  cm<sup>-3</sup>). In this range, it is equal to  $\frac{H_{\frac{3}{2}}(n)}{F_0(n)} = 0.67$  and this leads to  $\frac{\mu_{ev}}{\mu_{ec}} = 4.9$  in fair agreement with the experimental mobility ratio  $\frac{\mu_{ep}}{\mu_{en}} = 3.3$  derived from Table I. This comparison underlines the strong influence of the effective mass on the respective electronic mobility in *p*- and *n*-type Fe<sub>2</sub>VAl. Finally, the calculated  $PF(n)$  reaches a large  $PF_{\max} = 6.8$  mW m<sup>-1</sup> K<sup>-2</sup> at  $n_{\text{opt}} = 1.0 \pm 0.2 \times 10^{21}$  cm<sup>-3</sup> (Fig. 4(b)). This large value of the optimum electron concentration when compared to other thermoelectric materials is directly related to the large density of states effective mass for the conduction band: in *n*-type PbTe  $m^* = 0.5m_e$  and  $n_{\text{opt}} = 4 \times 10^{19}$  cm<sup>-3</sup> [49], in *n*-type CoSb<sub>3</sub>  $m^* = 3.2m_e$  and  $n_{\text{opt}} = 2 \times 10^{20}$  cm<sup>-3</sup> [38], and in *p*-type FeNbSb  $m^* = 10m_e$  and  $p_{\text{opt}} = 10^{21}$  cm<sup>-3</sup>. It is also approximately three times larger than the intrinsic hole concentration  $p_{\text{int}}$  and it thus makes the optimization of *n*-type Fe<sub>2</sub>VAl easier than its *p*-type counterpart. The composition Fe<sub>2</sub>V<sub>1.03</sub>Al<sub>0.97</sub> is indeed nearly optimized in the present work since it displays  $PF = 6.6$  mW m<sup>-1</sup> K<sup>-2</sup> at 220 K for  $n = 1.4 \times 10^{21}$  cm<sup>-3</sup>. As already discussed in the introduction, such large values of power factor have also been reported in Fe<sub>2</sub>V<sub>1.05</sub>Al<sub>0.95</sub> [17] and in Fe<sub>1.98</sub>V<sub>1.02</sub>Al<sub>0.9</sub>Si<sub>0.1</sub> [11] but with no measurements of the electron concentration.  $PF$  in *n*-type Fe<sub>2</sub>V<sub>1+x</sub>Al<sub>1-x</sub> is now fully optimized.

#### IV. CONCLUSIONS

Maximum power factor values  $PF = 3.2$  mW m<sup>-1</sup> K<sup>-2</sup> and  $PF = 6.7$  mW m<sup>-1</sup> K<sup>-2</sup> are found at 325 and at 250 K

in *p*- and *n*-type Fe<sub>2</sub>V<sub>1+x</sub>Al<sub>1-x</sub>, respectively. The following values of density of states effective mass are derived from fits of a parabolic band model to experimental Ioffe-Pisarenko plots for these compounds:  $m_v^* = 3.2m_e$  and  $m_c^* = 13.7m_e$  for the holes and electrons, respectively. The values of DOS mass in good agreement with the experimental ones are obtained from DFT calculations in *p*-type Fe<sub>2</sub>V<sub>0.96</sub>Al<sub>1.04</sub> and *n*-type Fe<sub>2</sub>V<sub>1.04</sub>Al<sub>0.96</sub>:  $m_v^* = 2.4m_e$  and  $m_c^* = 13.0m_e$ . A larger Sommerfeld coefficient of the electronic specific heat is measured in *n*-type Fe<sub>2</sub>V<sub>1.07</sub>Al<sub>0.93</sub> than in *p*-type Fe<sub>2</sub>V<sub>0.92</sub>Al<sub>1.08</sub>, consistent with the respective charge carrier effective masses. On the one hand, comparison of the parabolic band model with experimental power factor data shows that optimization of the latter in *p*-type Fe<sub>2</sub>V<sub>1+x</sub>Al<sub>1-x</sub> would require the synthesis of a sample with a hole concentration  $p_{\text{opt}} = 1.3 \pm 0.3 \times 10^{20}$  cm<sup>-3</sup>, a value two to three times smaller than the lowest values experimentally achieved in the literature, due to too large concentrations of antisite defects. On the other hand, the same comparison shows that *n*-type Fe<sub>2</sub>V<sub>1.03</sub>Al<sub>0.97</sub> which displays  $PF = 6.6$  mW m<sup>-1</sup> K<sup>-2</sup> for  $n = 1.4 \times 10^{21}$  cm<sup>-3</sup> is optimized. This difference between *p*-type and *n*-type conduction in Fe<sub>2</sub>V<sub>1+x</sub>Al<sub>1-x</sub> is of course related to the different effective mass of their charge carriers [50].

#### ACKNOWLEDGMENTS

The authors thank D. Bérardan for access to a PPMS at University Paris-Saclay. Funding of this work by the “Agence Nationale de la Recherche” through the contract “LoCoThermH” (Project No. ANR-18-CE05-0013-01) is also acknowledged.

- 
- [1] L. E. Bell, *Science* **321**, 1457 (2008).
- [2] J. R. Salvador, in *Thermoelectric Energy Conversion*, edited by R. Funahashi (Woodhead Publishing, Cambridge, 2021), pp. 609–632.
- [3] H. Mamur, M. R. A. Bhuiyan, F. Korkmaz, and M. Nil, *Renewable Sustainable Energy Rev.* **82**, 4159 (2018).
- [4] L. Yang, Z.-G. Chen, M. Hong, G. Han, and J. Zou, *ACS Appl. Mater. Interfaces* **7**, 23694 (2015).
- [5] H. J. Goldsmid, *Materials* **7**, 2577 (2014).
- [6] Y. Nishino, S. Deguchi, and U. Mizutani, *Phys. Rev. B* **74**, 115115 (2006).
- [7] E. Alleno, *Metals* **8**, 864 (2018).
- [8] K. Renard, A. Mori, Y. Yamada, S. Tanaka, H. Miyazaki, and Y. Nishino, *J. Appl. Phys.* **115**, 033707 (2014).
- [9] F. Garmroudi, M. Parzer, A. Riss, N. Reumann, B. Hinterleitner, K. Tobita, Y. Katsura, K. Kimura, T. Mori, and E. Bauer, *Acta Mater.* **212**, 116867 (2021).
- [10] S. Masuda, K. Tsuchiya, J. Qiang, H. Miyazaki, and Y. Nishino, *J. Appl. Phys.* **124**, 035106 (2018).
- [11] Y. Nishino and Y. Tamada, *J. Appl. Phys.* **115**, 123707 (2014).
- [12] F. Garmroudi, M. Parzer, A. Riss, A. V. Ruban, S. Khmelevskiy, M. Reticioli, M. Knopf, H. Michor, A. Pustogow, T. Mori, and E. Bauer, *Nat. Commun.* **13**, 3599 (2022).
- [13] F. Garmroudi, A. Riss, M. Parzer, N. Reumann, H. Müller, E. Bauer, S. Khmelevskiy, R. Podlucky, T. Mori, K. Tobita, Y. Katsura, and K. Kimura, *Phys. Rev. B* **103**, 085202 (2021).
- [14] A. Diack-Rasselio, O. Rouleau, L. Coulomb, L. Georgeton, M. Beaudhuin, J. C. Crivello, and E. Alleno, *J. Alloys Compd.* **920**, 166037 (2022).
- [15] S. Anand, R. Gurunathan, T. Soldi, L. Borgsmiller, R. Orenstein, and G. J. Snyder, *J. Mater. Chem. C* **8**, 10174 (2020).
- [16] F. Garmroudi, M. Parzer, A. Riss, S. Beyer, S. Khmelevskiy, T. Mori, M. Reticioli, and E. Bauer, *Mater. Today Phys.* **27**, 100472 (2022).
- [17] H. Miyazaki, S. Tanaka, N. Ide, K. Soda, and Y. Nishino, *Mater. Res. Express* **1**, 015901 (2014).
- [18] S. Maier, S. Denis, S. Adam, J.-C. Crivello, J.-M. Joubert, and E. Alleno, *Acta Mater.* **121**, 126 (2016).
- [19] D. Bérardan, E. Alleno, C. Godart, O. Rouleau, and J. Rodriguez-Carvajal, *Mater. Res. Bull.* **40**, 537 (2005).
- [20] O. Rouleau and E. Alleno, *Rev. Sci. Instrum.* **84**, 105103 (2013).
- [21] G. Kresse and J. Furthmüller, *Comput. Mater. Sci.* **6**, 15 (1996).
- [22] G. Kresse and J. Furthmüller, *Phys. Rev. B* **54**, 11169 (1996).
- [23] P. E. Blöchl, *Phys. Rev. B* **50**, 17953 (1994).
- [24] G. Kresse and D. Joubert, *Phys. Rev. B* **59**, 1758 (1999).
- [25] J. P. Perdew, K. Burke, and M. Ernzerhof, *Phys. Rev. Lett.* **77**, 3865 (1996).

- [26] J. P. Perdew, K. Burke, and M. Ernzerhof, *Phys. Rev. Lett.* **78**, 1396(E) (1997).
- [27] H. J. Monkhorst and J. D. Pack, *Phys. Rev. B* **13**, 5188 (1976).
- [28] A. Berche and P. Jund, *Materials (Basel)* **11**, 868 (2018).
- [29] A. Berche, M. T. Noutack, M. L. Doublet, and P. Jund, *Mater. Today Phys.* **13**, 100203 (2020).
- [30] J. de Boor, A. Berche, and P. Jund, *J. Phys. Chem. C* **124**, 14987 (2020).
- [31] S. Bandaru and P. Jund, *Phys. Status Solidi* **254**, 1600441 (2017).
- [32] V. I. Fistul', in *Heavily Doped Semiconductors*, edited by V. I. Fistul (Springer, New York, 1969), pp. 77–205.
- [33] K. Ellmer, *J. Phys. D* **34**, 3097 (2001).
- [34] B. Nag, in *Electron Transport in Compound Semiconductors* edited by B. Nag (Springer, Berlin, 1980), pp. 171–229.
- [35] G. S. Nolas, J. Sharp, and H. J. Goldsmid, *Thermoelectrics: Basic Principles and New Materials Developments* (Springer, Berlin, 2001).
- [36] T. Ishibe, A. Tomeda, K. Watanabe, Y. Kamakura, N. Mori, N. Naruse, Y. Mera, Y. Yamashita, and Y. Nakamura, *ACS Appl. Mater. Interfaces* **10**, 37709 (2018).
- [37] H. Miyazaki, K. Renard, M. Inukai, K. Soda, and Y. Nishino, *J. Electron Spectrosc. Relat. Phenom.* **195**, 185 (2014).
- [38] M. Benyahia, V. Ohorodniichuk, E. Leroy, A. Dauscher, B. Lenoir, and E. Alleno, *J. Alloys Compd.* **735**, 1096 (2018).
- [39] E. Alleno, M. Benyahia, J. B. Vaney, K. Provost, V. Paul-Boncour, J. Monnier, A. Dauscher, and B. Lenoir, *J. Mater. Chem. C* **8**, 17034 (2020).
- [40] H. Xie, H. Wang, Y. Pei, C. Fu, X. Liu, G. J. Snyder, X. Zhao, and T. Zhu, *Adv. Funct. Mater.* **23**, 5123 (2013).
- [41] C. Fu, T. Zhu, Y. Pei, H. Xie, H. Wang, G. J. Snyder, Y. Liu, Y. Liu, and X. Zhao, *Adv. Energy Mater.* **4**, 1400600 (2014).
- [42] Y. Nishino, *IOP Conf. Ser.: Mater. Sci. Eng.* **18**, 142001 (2011).
- [43] P. M. Chaikin, in *Organic Superconductivity*, edited by V. Z. Kresin and W. A. Little, (Plenum Press, New York, 1990).
- [44] H. Ibach and H. Lüth, *Solid-State Physics: An Introduction to Principles of Materials Science* (Springer, Berlin, 2009).
- [45] C. S. Lue, J. H. Ross, C. F. Chang, and H. D. Yang, *Phys. Rev. B* **60**, R13941 (1999).
- [46] H. Michor, T. Holubar, C. Dusek, and G. Hilscher, *Phys. Rev. B* **52**, 16165 (1995).
- [47] J. I. Lee, T. S. Zhao, I. G. Kim, B. I. Min, and S. J. Youn, *Phys. Rev. B* **50**, 4030 (1994).
- [48] M. S. T. Noutack, A. Diack-Rasselio, E. Alleno, and P. Jund, *J. Alloys Compd.* **883**, 160828 (2021).
- [49] Y. Pei, Z. M. Gibbs, A. Gloskovskii, B. Balke, W. G. Zeier, and G. J. Snyder, *Adv. Energy Mater.* **4**, 1400486 (2014).
- [50] [https://en.wikipedia.org/wiki/RGB\\_color\\_model](https://en.wikipedia.org/wiki/RGB_color_model), (2022).